Modeling the Spectral Energy Distributions and Spectropolarimetry of Blazars—Application to 4C+01.02 in 2016–2017[*]

Hester M. Schutte[1] , Richard J. Britto[2] , Markus Böttcher[1] , Brian van Soelen[2] , Johannes P. Marais[2] , Amanpreet Kaur[3] ,
Abraham D. Falcone[3] , David A. H. Buckley[2,4] , Andry F. Rajoelimanana[2] , and Justin Cooper[2]

[1] Centre for Space Research, North-West University, Potchefstroom 2520, South Africa; schuttehester1@nwu.ac.za
[2] Department of Physics, University of the Free State, Bloemfontein 9300, South Africa; dr.richard.britto@gmail.com
[3] Department of Astronomy and Astrophysics, Pennsylvania State University, University Park, PA 16802, USA
[4] South African Astronomical Observatory, Observatory, Cape Town 7935, South Africa
Received 2021 May 13; revised 2021 November 10; accepted 2021 November 22; published 2022 February 1

Abstract

The optical radiation emitted by blazars contains contributions from synchrotron radiation by relativistic electrons in the jets, as well as thermal radiation emitted mainly by the accretion disk (AD), the broad-line region (BLR), and the host galaxy. The unpolarized radiation components from the AD, BLR, and host galaxy present themselves by decreasing the total polarization in the optical/ultraviolet (UV) spectrum. A combined model for the spectral energy distribution (SED) and degree of optical/UV polarization is constructed, enabling the disentanglement of the synchrotron and AD components. Our model is applied to the multiwavelength SED and spectropolarimetry observations of the flat-spectrum radio quasar 4C+01.02 ($z = 2.1$) in its 2016 July–August flaring state and 2017 July–August quiescent state, using data from the Fermi Large Area Telescope, the Southern African Large Telescope, and the Las Cumbres Observatory network of telescopes. By constraining the AD component, the mass of the supermassive black hole is obtained as $\sim 3 \times 10^9 M_\odot$. Furthermore, the model retrieves the characteristics of the relativistic electron distribution in the jet and the degree of ordering of the magnetic field. Our results highlight the potential of spectropolarimetry observations for disentangling thermal from nonthermal (jet) emission components, thus revealing the physics of particle acceleration and high-energy emission in active galactic nucleus jets.

Unified Astronomy Thesaurus concepts: Active galaxies (17); Galaxy jets (601); Flat-spectrum radio quasars (2163); Spectropolarimetry (1973); Blazars (164); Active galactic nuclei (16)

Supporting material: data behind figures

1. Introduction

Blazars are a class of jet-dominated (radio-loud) active galactic nuclei (AGNs) in which one of the jets is closely aligned with our line of sight, leading to a strongly Doppler-boosted emission received by the observer. They can be subdivided into two classes, namely, flat-spectrum radio quasars (FSRQs) and BL Lac objects, which are distinguishable by the visibility of their emission-line features in optical spectra: FSRQs have broad emission lines (equivalent width >5 Å) while BL Lacs have weak or absent emission lines (Stickel et al. 1991). Blazars are characterized by rapid variability across the electromagnetic spectrum and a high degree of polarization in the radio and optical regime.

The detection of significantly polarized optical emission from many blazars indicates that it originates dominantly from synchrotron radiation (Rybicki & Lightman 1986; Smith et al. 1986). Additional, unpolarized emission components arising from the dust torus (infrared, IR), host galaxy (optical), broad-line region (BLR), and accretion disk (AD) (optical–optical/ultraviolet (UV)–X-rays) may also contribute to the observed radiation. The AD is directly visible in a few blazars but is often outshone by the nonthermal jet synchrotron continuum.

The high-energy spectral energy distribution (SED) components in the X-ray through gamma-ray energy bands can be modeled with leptonic or hadronic models (Böttcher et al. 2013). Both these models provide Compton scattering components in the X-ray through the gamma-ray spectrum, which are, however, often subdominant in the case of hadronic models. Specifically, they have in common a synchrotron self-Compton (SSC) component where electrons Compton-upscatter synchrotron photons previously produced by the same population of electrons.

In the leptonic model, leptons (electrons and possibly positrons) dominate the electromagnetic (EM) radiation. It is possible for protons to be present in the emission region, but protons are assumed not to be accelerated to sufficiently high energies to provide a significant radiative output. The contributions of protons are included when studying the kinetic jet power, which may still be dominated by protons due to their larger rest mass compared to electrons/positrons. In the leptonic model, the high-energy emission can be produced through both SSC and external Compton (EC) scattering of low-energy seed photons from the AD, dust torus, and the BLR (Marscher & Gear 1985; Dermer & Schlickeiser 1993; Sikora et al. 1994).

In the hadronic model, electron synchrotron emission dominates at low frequencies, and protons are assumed to be accelerated to sufficiently high energies to radiate appreciably. In the X-ray through gamma-ray regime, radiation is produced by photopion interactions yielding EM particle cascades ($p + \gamma \rightarrow \pi^0 + p$ or $p + \gamma \rightarrow n + \pi^+$). In the strong ($\sim 10$–$100$ G)

magnetic fields required for hadronic models, ultrarelativistic protons are also efficiently radiating proton-synchrotron radiation (Mannheim 1993; Aharonian 2000; Mücke et al. 2003).

SED modeling leaves many parameter degeneracies, which can be constrained by including polarization information. Spectropolarimetric observations of blazars are particularly useful for this purpose. Such spectropolarimetric observing campaigns are currently being conducted by several groups and at several observatories, including the Southern African Large Telescope (SALT). Ongoing Target of Opportunity (ToO) spectropolarimetry and spectroscopy observations of blazars are conducted via a SALT Large Science Proposal.

In this paper, we discuss and interpret observations of the FSRQ 4C+01.02 (also known as PKS B0106+013; ICRS coord. (ep=J2000): $\alpha = 01^h\, 08^m\, 38\overset{s}{.}77$, $\delta = +01°\, 35'00''.32$ (optical); Gaia Collaboration 2018), located at a redshift $z = 2.1$ (Pâris et al. 2018).

This source exhibited its brightest flare ever recorded in gamma rays in 2016 July–August (Verrecchia et al. 2016). Based on this event, we monitored the source at multiwavelengths for several months and observed it again in 2017 July–August to uncover the source radiation during a low state.

The SEDs of FSRQs are often successfully interpreted in the framework of leptonic models (Meyer et al. 2012). The FSRQ 4C+01.02 has previously been studied by Ghisellini et al. (2011) and Paliya et al. (2017) who determined its black hole (BH) mass as $5 \times 10^9\, M_\odot$. The BH mass estimate by Ghisellini et al. (2011) stemmed from a fit to the optical regime in the SED that was strongly dominated by direct AD emission and thus expected to yield low degrees of polarization. However, during flaring states, the synchrotron emission is sufficiently dominant to produce a significant degree of total polarization. The transition from low-polarization AD-dominated emission to synchrotron-dominated high-polarization emission is accessible to spectropolarimetry and provides an important constraint unavailable with the SED alone. We have detected such a transition in spectropolarimetric observations with SALT, motivating a joint fit to the SED and the spectropolarimetry.

In our model, the spectropolarimetry observations are fitted simultaneously with the SED to disentangle the spectrum of the synchrotron and AD components and thereby, indirectly, constraining the mass of the BH. Constraints from spectropolarimetry observations were not considered in most previous blazar models (for the inclusion of spectropolarimetry observations in the modeling of the FSRQ 3C 345, see Smith et al. 1986).

In this paper, the observations of 4C+01.02 during its flaring (2016 July–August) and quiescent (2017 July–August) states are described in Section 2. A simultaneous SED and spectropolarimetry model is constructed for blazars in the optical/UV regime in Section 3. The model is compared with the observations, and the results are shown in Section 4. A summary and conclusion of the significance of including spectropolarimetry observations are discussed in Section 5. Throughout this paper, we use cosmological parameters $\Omega_\Lambda = 0.7$, $\Omega_m = 0.3$, and $H_0 = 70\, \mathrm{km\, s^{-1}\, Mpc^{-1}}$. With these parameters, the redshift of $z = 2.1$ corresponds to a luminosity distance of $d_L = 4.952 \times 10^{28}$ cm.

2. Observations

In this section we describe the observations we conducted in the optical band with the Las Cumbres Observatory (LCO) network of telescopes and the SALT. We also describe our analysis of data from the Swift X-Ray Telescope (XRT) and the Large Area Telescope on board the Fermi Gamma Ray Space Observatory (Fermi-LAT) in the MeV–GeV domain. Radio through UV archival data were taken from the NED (http://ned.ipac.caltech.edu/), WISE (https://irsa.ipac.caltech.edu), GALEX (http://galex.stsci.edu/GR6/).

2.1. Photometry with LCO

The Las Cumbres Observatory (LCO)[5] was used to obtain photometric observations of 4C+01.02 in the B, V, and R bands during MJD 57602–57605 and MJD 57626–57643, covering parts of the 2016 July–August gamma-ray outburst (see Section 2.4). Observations on 2016 August 2 (MJD 57602.3301–57602.3350) were used to model the optical flux during the flaring state. A set of four observations (B, V, R, and I filters) was also taken on 2017 July 28 (MJD 57962.1671–57962.1796) in order to model the optical flux during quiescence. Standard prereduction was done with the BANZAI pipeline,[6] and the apparent magnitude was calibrated using the SDSS magnitudes of the nearest 10 comparison sources in the field of view, converted to the Johnson–Cousin magnitudes using Jordi et al. (2006).

2.2. Optical Spectropolarimetry with SALT

Optical spectropolarimetry observations of 4C+01.02 were carried out on 2016 July 9 (MJD 57578.1354–57578.1638) and on 2017 July 25 (MJD 57959.1062–57959.1347) using the Robert Stobie Spectrograph (RSS) on SALT (Buckley et al. 2006; Kobulnicky et al. 2003; Burgh et al. 2003; Nordsieck 2012; Brink et al. 2010; Potter et al. 2016). Observations were taken in LINEAR mode using the pg0300 grating at a grating angle of 5°.37 with an exposure time of 2400 s (600 s per half-wave plate angle). The observations covered a wavelength range of ~3200–8500 Å with a resolving power of $R \sim 167$–533. The prereduction, wavelength calibration, and polarization measurement were done using the POLSALT reduction pipeline version 20171226 (`specpolextract_dev 20180524`), based on pySALT v0.5dev.[7] The normalized counts spectrum and degree of polarization are shown in Figure 1.

The 2016 July 9 data were obtained where 4C+01.02 was close to the maximum of its outburst in that year, during the phase we labeled as "Flare" or "Main flare" in Section 2.4. On the other hand, the 2017 July 25 observation corresponds to a quiescent episode that lasted for several months in 2017. Because the continuum emission was fainter in 2017, emission lines appear more prominent in the figure. Thanks to the high redshift of the source ($z = 2.1$), prominent ultraviolet emission lines Lyα 1216 Å, Si IV 1400 Å, C IV 1549 Å, and C III 1909 Å were observed in the 3700–6000 Å range. However, because the Lyα 1216 Å line was only visible at the extreme blue end of the spectrum where the count rate is low and the spectrum is noisy, it has not been included in Figure 1.
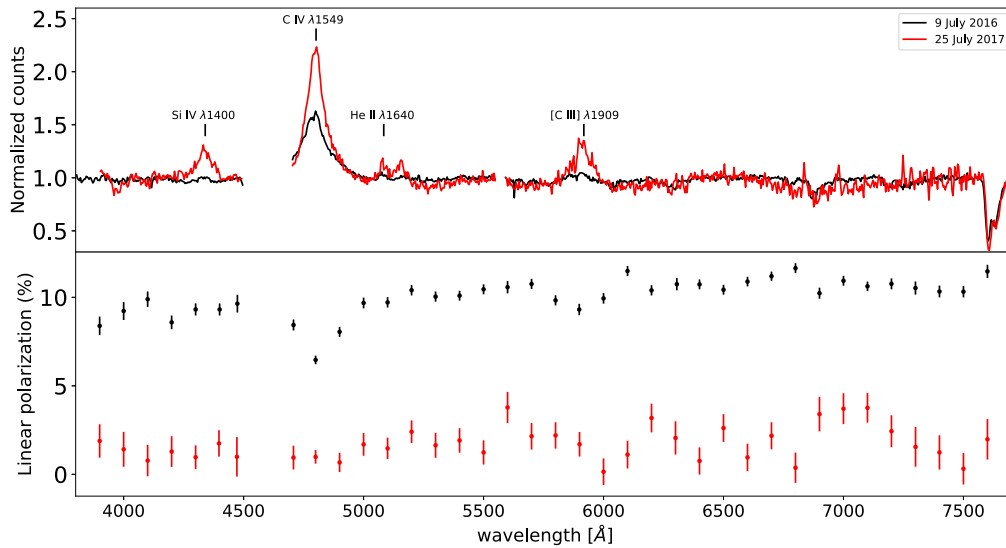

Figure 1. Optical spectropolarimetry data of 4C+01.02 taken on 2016 July 9 (black) and 2017 July 25 (red). Top: normalized intensity spectra. Bottom: degree of linear polarization in 100 Å bins. The gap in the spectrum around 4700 Å is due to the gap between the RSS CCDs, while the smaller gap around 5570 Å is a region excluded due to contamination from a sky line. The optical spectropolarimetry is available as the data behind the figure.

(The data used to create this figure are available.)

Table 1
Spectral Parameters, Integral Flux, and Significance of the Spectral Curvature Obtained from the Analysis of the Fermi-LAT Data over the Four Periods of the 2016 Outburst, and the 2017 Quiescent Period

Period	Γ_{PL}	α	β	$F(0.1 - 300 \text{ GeV}) (10^{-7} \text{ ph cm}^{-2} \text{ s}^{-1})$	TS_{curv}
2016 May 11–May 28 (Preflare)	2.26 ± 0.06	2.04 ± 0.09	0.19 ± 0.06	5.3 ± 0.4	12.9
2016 May 28–July 2 (Plateau)	2.36 ± 0.03	2.27 ± 0.04	0.11 ± 0.03	9.9 ± 0.3	34.5
2016 July 2–July 20 (Flare)	2.26 ± 0.03	2.11 ± 0.04	0.16 ± 0.03	15.6 ± 0.6	22.4
2016 July 20–August 15 (Postflare)	2.41 ± 0.03	2.32 ± 0.04	0.12 ± 0.03	13.8 ± 0.4	9.4
2017 July 3–August 2 (Quiescent)	2.35 ± 0.10	2.00 ± 0.15	0.28 ± 0.09	0.9 ± 0.1	5.0

Note. We model the spectral shape of 4C+01.02 by a power-law function (PL, characterized by the photon index Γ_{PL}), then by a log-parabola (LP, characterized by the α and β parameters). The integral flux F was determined using the LP model. The TS_{curv} parameters represent the test statistics ($\sim \sigma^2$) of the spectral curvature of the SED.

A spectrum in the 3000–8500 Å range was also taken with the SpUpNIC spectrograph on the SAAO 1.9 m telescope[8] on 2016 August 1 (MJD 57601.10, during the "postflare" period; see Table 1), which confirmed the identification of the optical lines mentioned above (Britto et al. 2017).

The degree of linear polarization is around 10% during the flare observation, and between 1% and 2% during the quiescent state, which agrees with the prediction that strongly polarized synchrotron emission is released by blazars during outburst episodes.

The unpolarized star GAIA 2538240223562516480 (apparent magnitude $G = 16.32$; distance $= 491$ pc) was observed in the spectrograph's slit of 4C+01.02 on 2017 July 25. The data reduction of this comparison/reference star yields a linear polarization degree below 1% for most of the binned data points above 4800 Å. This allows us to estimate a systematic uncertainty on the measurement of the linear polarization degree.

2.3. X-Ray Observations with Swift-XRT

Launched on 2004 November 20, the Neil Gehrels Swift Observatory (Swift; Gehrels et al. 2004) is a NASA-led space observatory. One of its three instruments, the X-Ray Telescope (XRT; Burrows et al. 2005), is sensitive to soft X-ray photons.

Because no X-ray observations were performed during the 2016 flaring period, we included the Swift-XRT SED from Ghisellini et al. (2011), built from summed observations from 2007 July 2, 2008 January 10, 2008 February 16, and 2009 August 16, obtained in the 0.2–10 keV range. By considering both the lack of outburst reports and the monitoring of this source from Fermi-LAT since August 2008, we can consider that these XRT data represent a moderate quiescent-state level of 4C+01.02, and we used them as a lower limit guide in our fit of the broadband SED of the 2016 flaring period.

For the quiet state of the source in 2017, we used Swift-XRT data taken on 2017 August 2 (MJD 57967.91), which corresponds to the end of the Fermi-LAT quiescent observation period (2017 July 3–August 2). The cleaned level 3 event files[9] generated by xrtpipeline-v.0.13.4 were utilized to
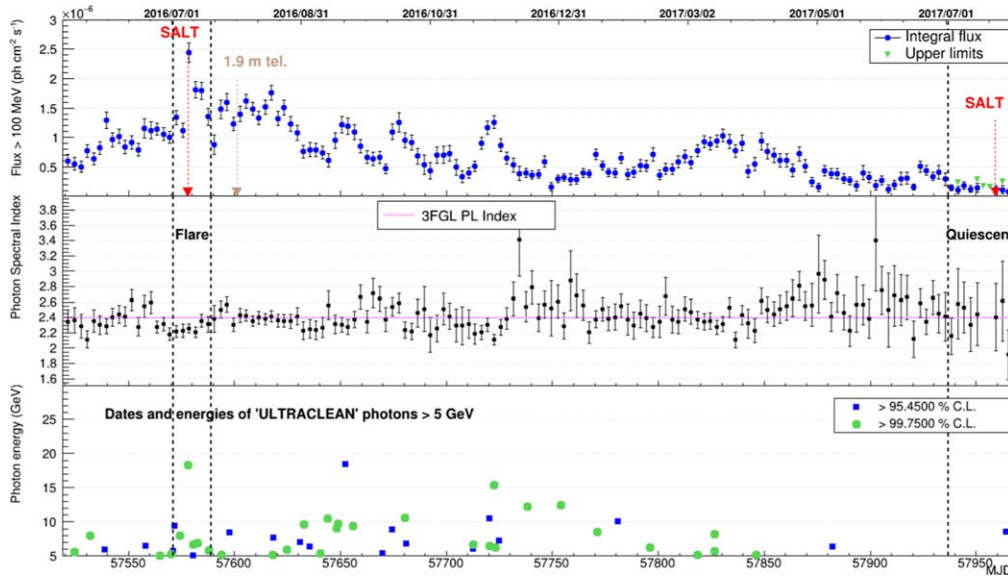
Figure 2. Top: Fermi-LAT light curve of 4C+01.02 above 100 MeV between 2016 May 11 and 2017 August 2 in a three-day binning. Middle: corresponding values of the modeled power-law spectral index of 4C+01.02. Bottom: energy and date of individual high-energy events identified as photons from 4C+01.02 with a high probability. The flare and quiescent periods, corresponding to the 2016 July 2–20 and 2017 July 3–August 2 time ranges, respectively, are delimited by black dashed vertical lines.

generate the image and spectrum within the 0.3–10.0 keV energy range using the XSELECT package from HEASoft v.6.26. The cleaned level 3 event files[10] generated by xrtpipeline-v.0.13.4 were utilized to generate the image and spectrum within the 0.3–10.0 keV energy range using the XSELECT package from HEASoft v.6.26.0. First, a circular source region of size 20 pixels and an annular background region of size 50 pixels were chosen to extract the spectrum. The exposure maps created by the xrtpipline-v.0.13.4 were then used to generate the Ancilliary Response File, i.e., the arf file employing the xrtmkarf command. The Response Matrix File, i.e., the rmf file used in this process, was later used for grouping all these spectral files, using the grppha command.

Xspec v.12.10.0 c was employed to fit the grouped spectrum with a simple power-law (PL) model absorbed by the Tuebingen–Boulder interstellar medium (ISM) absorption model using the form: tbabs*powerlaw.

During the fitting procedure, the gas column density between the source and the observer was fixed to the Galactic hydrogen density $N_H = 2.42 \times 10^{20}$ cm^{-2}. This was derived from the LAB survey (Kalberla et al. 2005) using the online nH tool.[11] The goodness of the fit was evaluated by using C-statistic, resulting in C $-$ Stat $= 53.52$ for 41 degrees of freedom (Cash 1979). The available data were limited to the energy range 0.45–6.0 keV. The final fit yielded an unabsorbed flux of $F_{0.45-6\,keV} = 1.19 \times 10^{-12}$ erg cm^{-2} s^{-1} corresponding to a PL with a photon index of 1.43 ± 0.23.

2.4. Gamma-Ray Observations with Fermi-LAT

The Fermi Gamma-Ray Space Telescope has been orbiting Earth since 2008 June. It operates in survey mode most of the time, covering the whole sky every 3 hr (corresponding to two orbits), thanks to its large (∼2.4 sr) field of view. Following the

2018 March 16 solar panel drive anomaly, at some Sun angles, some sources may receive less exposure on 1 week time-scales.[12] This allows regular monitoring of sources on the whole sky. Its main instrument, the Large Area Telescope (LAT), is sensitive to photons from ∼20 MeV to several hundreds of GeV (Atwood et al. 2009).

We present the analysis of Fermi-LAT data from 2016 May until 2017 October, in the 100 MeV–300 GeV range. We used the Pass8 (R2) data set (Atwood et al. 2013) and the Fermi Science Tools version v10r0p5.[13] We performed both time domain and spectral analysis by running the unbinned likelihood algorithm (gtlike/pyLikelihood Science Tool) with the following standard analysis cuts applied to point-source analysis: radius of the region of interest (ROI)=15°; source region: a 10° annulus surrounding the ROI; SOURCE class; event type = 3; zenith angle < 90°; DATA_QUAL=1, LAT_CONFIG=1; diffuse emission templates: gll_iem_v06.fits (Galactic) and iso_P8R2_SOURCE_V6_v06.txt (isotropic). The spectrum of the source of interest was successively modeled by the two following functions: a log-parabola (LP—with its standard parameters α and β) and a single PL (with photon index Γ_{PL}), except while running the likelihood algorithm in narrow time or energy bins. Depending on the data set and analysis cuts, between 8 and 16 parameters defining the spectral shapes of the brightest point sources of the ROI and the spectral index of the two diffuse templates were kept free in the likelihood analysis.

We present in Figures 2 and 3 the three-day and daily light curves, respectively, of 4C+01.02 (top panel), the time evolution of the PL spectral index (middle panel), and the dates and energy of high-energy photons above 5 GeV, identified as gamma-rays and as emitted by 4C+01.02 with a probability >95.45% to originate from the target (bottom panel). According to the flux level and variability pattern, we defined four episodes that we referred to as preflare, plateau,
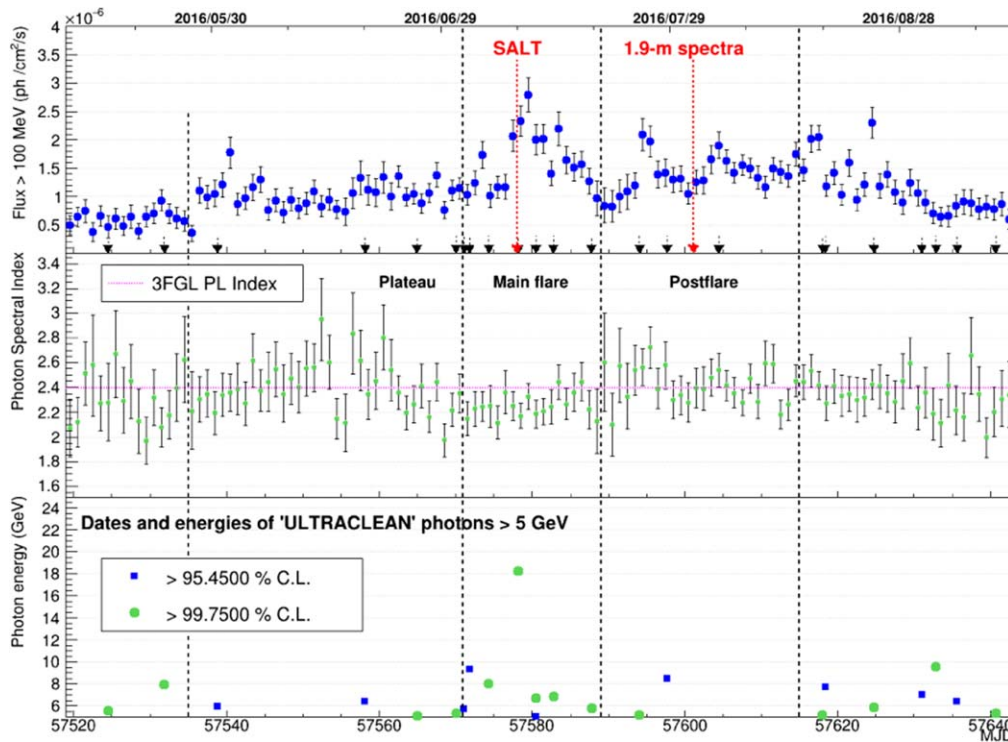
Figure 3. Top: Fermi-LAT light curve of 4C+01.02 above 100 MeV between 2016 May 11 and September 12 in a one-day binning. Middle: corresponding values of the modeled power-law spectral index of 4C+01.02. Bottom: energy and date of individual high-energy events identified as photons from 4C+01.02 with a high probability. The preflare, plateau, flare, and postflare periods, corresponding to the 2016 May 11–28, 2016 May 28–July 2, 2016 July 2–20, and 2016 July 20–August 15 time ranges, respectively, are delimited by black dashed vertical lines.

(main) flare, and postflare, successively. In Table 1 we present the spectral parameters that we obtained in our analysis of each of these four episodes and the 2017 subset of the quiescent state, using successively the PL and LP functions to model the spectral shape of 4C+01.02. The plateau–flare–postflare pattern was previously observed for FSRQ 3C 454.3 during several of its outbursts (e.g., Abdo et al. 2011; Britto et al. 2016 and references therein).

In Figure 3, the epochs of the SALT and SAAO observations are highlighted with red arrows. The variation of the spectral photon index $\Gamma_{\rm PL}$ (middle panel) suggests a hardening of the SED when the source is brighter—during the main flare. This is a common feature reported for bright FSRQs during outbursts. An unusual feature is that the preflare period (corresponding to a relatively quiescent state of the source) seems to be also characterized by a hardening of the spectrum, as also reported in Table 1.

This table also lists the test statistic that quantifies the presence of spectral curvature in the gamma-ray spectrum of the source. This was done by computing $\mathrm{TS}_{\rm curv}$ as follows:

$$\mathrm{TS}_{\rm curv} = -2 \times [\ln(\mathcal{L}_{\rm LP}) - \ln(\mathcal{L}_{\rm PL})], \qquad (1)$$

where $\ln(\mathcal{L}_{\rm LP})$ and $\ln(\mathcal{L}_{\rm PL})$ represent the natural logarithm of the maximum likelihood obtained with the LP and PL models, respectively. The preferred model is LP.

We show in Figure 4 a subset of the Fermi-LAT light curve of Figure 3, along with the LCO light curve obtained during the 2016 observation campaigns. The LCO data presented here include dereddening. However, the LCO observations were not continuous and most of the contemporaneous Fermi-LAT/ LCO monitoring was undertaken after the main flare when the variability of the source was not significant in gamma-rays. This prevented us from quantifying any time lag between the

different energy bands, though the visual inspection reveals that the peak positions around MJD 57604 appear without significant shift between the B, V, R and LAT bands. We also observe a flux decrease after MJD 57626 for all four bands. This observation suggests a single-zone origin of the optical and gamma-ray emissions.

Spectral analysis is presented for both the flare and quiescent periods (Figure 5). Fits were performed using both the PL and LP functions with all their parameters fixed to the values obtained from the unbinned likelihood analysis shown in Table 1. (SED data points were obtained using PL models for each point source in the ROI and source region.)

The estimated systematic uncertainty in the effective area is 5% in the 100 MeV–100 GeV range. The energy resolution ($\Delta E/E$, at 68% containment) is 20% at 100 MeV, and between 6% and 10% over the 1–500 GeV range.[14,15]

3. Model Setup

A model is constructed for blazars that simultaneously fits the low-energy (microwave through UV) component of the SED and the degree of polarization as a function of wavelength in the optical-UV regime. The simultaneous SED and polarization fit consists of the synchrotron, AD, and emission lines from the BLR flux components.

The host galaxy and dust torus emissions are considered negligible in the strongly jet-dominated IR–optical spectrum but can be included in the model in future work. The synchrotron flux is calculated from a broken PL, exponential
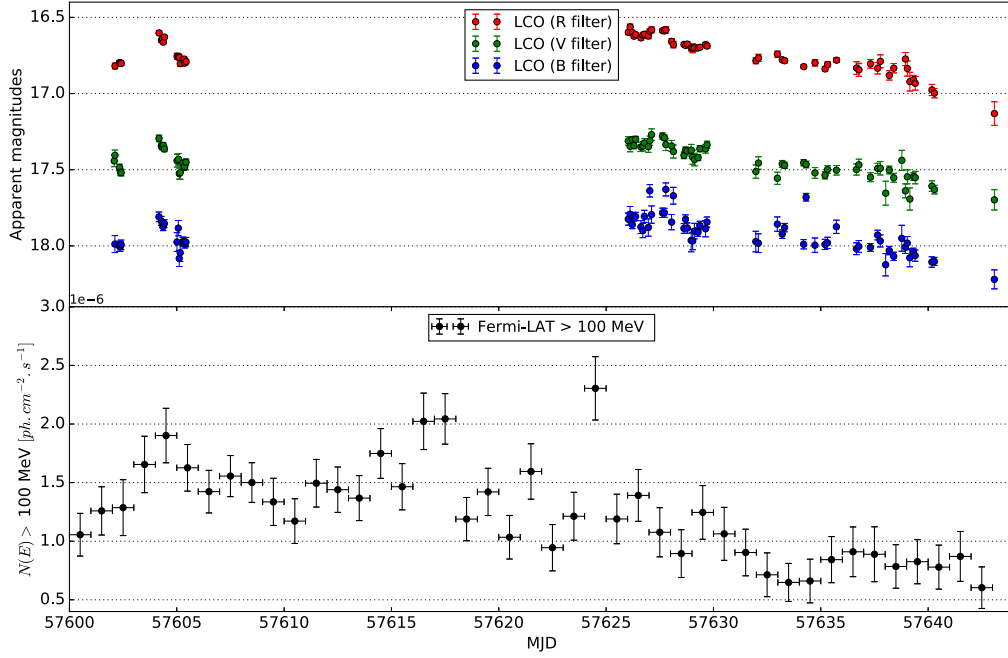

Figure 4. Top: LCO light curves in the *R*, *V*, and *B* bands (apparent magnitudes). This photometric data are available as the data behind the figure. Bottom: Fermi-LAT light curve in a one-day binning.
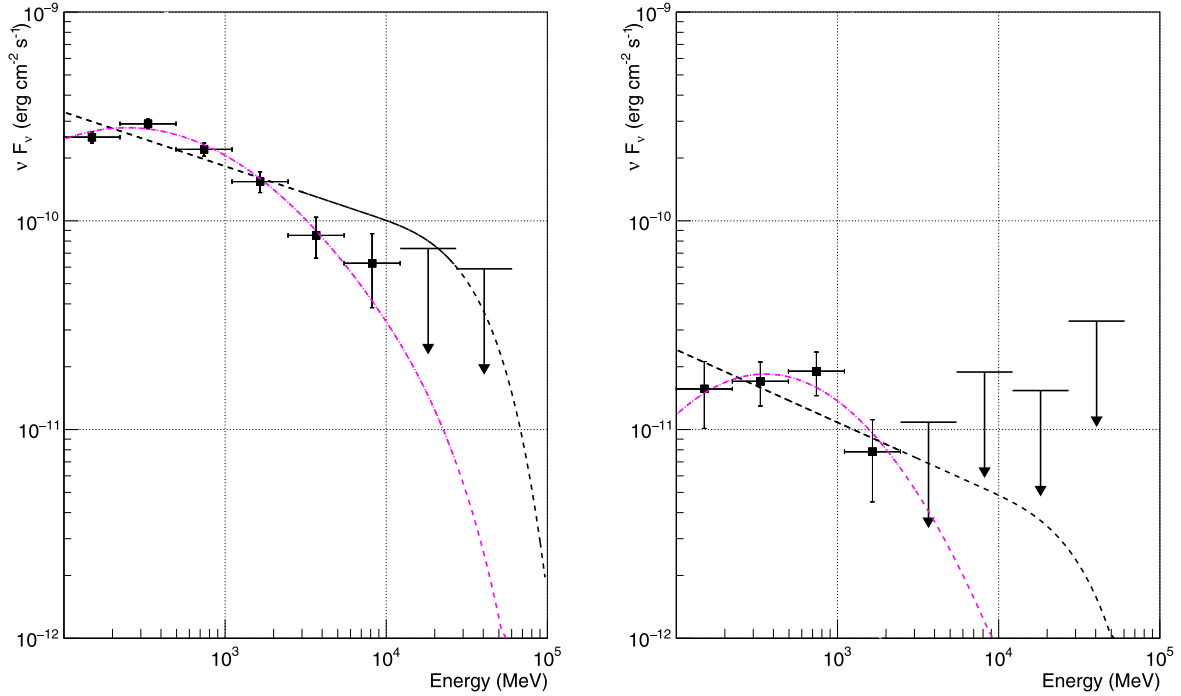
(The data used to create this figure are available.)

Figure 5. Fermi-LAT SED of 4C+01.02 during the "flare" (left) and "quiescent" (right) states. Data points are fitted by a PL (black dashed) and an LP (magenta dashed) function. The absorption by the extragalactic background light was modeled by the $e^{-\tau_{\gamma\gamma}(E)}$ factor applied to both functions and corresponding to the redshift $z = 2.1$, using the model developed by Finke et al. (2010).

cutoff electron distribution:

$$N_e(\gamma) = n_0 \begin{cases} \left(\dfrac{\gamma}{\gamma_b}\right)^{-p_1} \cdot e^{-\gamma_b/\gamma_c} & \text{for } \gamma_{\min} \leqslant \gamma \leqslant \gamma_b \\[2ex] \left(\dfrac{\gamma}{\gamma_b}\right)^{-p_2} \cdot e^{-\gamma/\gamma_c} & \text{for } \gamma_b < \gamma < \gamma_{\max} \end{cases}, \quad (2)$$

where n_0 is a normalization factor determining the total number of nonthermal electrons, γ_b and γ_c the characteristic break and cutoff energies in the comoving frame of the emission region, and p_1 and p_2 the electron spectral indices. The emission region is pervaded by a magnetic field B and moves along the jet with a bulk Lorentz factor Γ. To reduce the number of free parameters, we assume a viewing angle of $\theta_{\rm obs} = 1/\Gamma$ so that

the Doppler factor $\delta = (\Gamma[1 - \beta_\Gamma \cos \theta_{obs}])^{-1} = \Gamma$. Where the emission region becomes optically thick (at optical depth $\tau_{SSA} = R_{em} \cdot \alpha_{SSA} > 1$), the synchrotron emission is self-absorbed. Here, R_{em} is the emission region radius. The absorption coefficient α_{SSA} is calculated following Equation (6.50) of Rybicki & Lightman (1986). The synchrotron self-absorption (SSA) effect leads to a steepening of the spectrum below a critical SSA frequency where $\tau_{SSA} = 1$.

The Shakura & Sunyaev (1973) AD model is used for calculating the AD SED component. This model assumes a geometrically thin AD around a nonrotating BH for which the innermost stable orbit is $R_{in} = 3\,R_S$, with R_S the Schwarzschild radius. The outer boundary of the AD is assumed to be at radius $R_{out} = 10^3\,R_S$. Our results are insensitive to the exact choice of R_{out} as the cold disk at those radii no longer contributes significantly to the overall spectrum. At the inner disk radius, the maximum disk temperature is defined as

$$T^{AD,max} \propto l^{1/4} M_{BH}^{-1/4}, \qquad (3)$$

with $l = \frac{\dot{M}_{BH}}{\dot{M}_{Edd}} = \frac{L_{AD}}{L_{Edd}}$ being the Eddington ratio and the accretion rate $\dot{M}_{BH} = L_{AD}/(\epsilon c^2)$. The efficiency of converting potential energy into radiation is assumed as $\epsilon = 1/12$. The AD SED component peaks at a frequency that is related to this maximum temperature through

$$\nu^{AD,peak} = 2.8 \cdot kT^{AD,\,max}/h. \qquad (4)$$

The parameters determining $\nu^{AD,peak}$ are M_{BH} (increasing M_{BH} yields lower $\nu^{AD,peak}$), ϵ (increasing ϵ increases $\nu^{AD,peak}$ and yields higher νF_ν^{AD}), and $\dot{M}_{BH}$ (increasing $\dot{M}_{BH}$ increases $\nu^{AD,peak}$ and νF_ν^{AD}; Calderone et al. 2013).

Synchrotron polarization is calculated as

$$\Pi_\omega^{syn} = F_B \cdot \frac{\int N_e(\gamma) x(\gamma) K_{2/3}(x(\gamma)) d\gamma}{\int N_e(\gamma) x(\gamma) \int_{x(\gamma)}^{\infty} K_{5/3}(x(\xi)) d\xi d\gamma}, \qquad (5)$$

where F_B is the factor characterizing the ordering of the magnetic field and $x(\gamma) = \omega/\omega_c(\gamma)$, with $\omega_c(\gamma)$ the critical frequency (Westfold 1959). This parameterization of the magnetic field ordering has previously been used in Smith et al. (1986) and Zhang & Böttcher (2013). The Bessel functions $K_{2/3}$ and $K_{5/3}$ are computed with the Python in-built Bessel function besselk() from the mpmath package.

For a pure PL electron spectrum with index p (corresponding to a synchrotron radiation spectral index $\alpha = [p - 1]/2$), the degree of synchrotron polarization can be $\Pi_{max}^{syn} = \frac{p+1}{p+7/3} = \frac{\alpha+1}{\alpha+5/3}$ (Longair 2011). For spectral indices in the range $2 < p < 3$, the maximum degree of synchrotron polarization is $69\% < \Pi_{max}^{syn} < 75\%$. For a broken PL distribution, the synchrotron polarization is still approximately described by the above identities for frequencies sufficiently far away from (between) the spectral breaks/cutoffs. For a gradually steepening synchrotron spectrum (due to a broken/cutoff electron distribution), the synchrotron polarization increases toward higher frequencies, corresponding to an increasing value of α.

The total optical/UV flux is the sum of the polarized synchrotron and unpolarized AD and emission-line fluxes.

Hence, the total degree of polarization is given by

$$\Pi_\omega^{tot} = \frac{\Pi_\omega^{syn} \cdot F_\omega^{syn}}{F_\omega^{syn} + F_\omega^{AD} + F_\omega^{lines}}. \qquad (6)$$

In the model code, the unpolarized emission lines are approximated by Gaussian functions. The emission-line fluxes are calculated relative to each other and independently of the continuum flux (Francis et al. 1991).

A χ^2 minimization technique was employed to determine the best-fit parameters characterizing the nonthermal electron distribution, F_B, AD luminosity, and BH mass.

The broadband SED is subsequently obtained by employing the steady-state leptonic blazar model of Böttcher et al. (2013) with the nonthermal electron spectrum and magnetic field obtained from the low-frequency SED and spectropolarimetry fit described above. The SED and spectropolarimetry fit determine the density of radiating electrons. The characteristics of the external radiation field are adjusted to obtain a fit to the high-energy (X-ray through gamma ray) SED. The BLR target photon field is modeled as a thermal radiation field that is isotropic in the AGN rest frame with a characteristic temperature such that the resulting EC spectrum is a good representation of a BLR radiation field. For a comparison between using a detailed, line-dominated BLR radiation field and a thermal BLR, see Böttcher et al. (2013).

4. Results and Discussion

The model was fitted to contemporaneous LCO optical photometry and SALT spectropolarimetry data, complemented by archival radio through UV data of 4C+01.02 in its flaring state from 2016 and quiescent state from 2017. The fit was conducted over the SALT spectropolarimetry observations in the 3.9×10^{14} to 7.5×10^{14} Hz range. The results of this SED and spectropolarimetry fitting are discussed in Section 4.1. A fit of the broadband SED, including the high-energy (Compton) components produced with the code of Böttcher et al. (2013), is discussed in Section 4.2. We discuss and compare our results to those obtained in previous work in Section 4.3 and to the BH mass estimate based on the C IV line width and the continuum luminosity in Section 4.4.

The parameter results obtained by the model presented in this paper are indicated by a superscript M and appended by the superscripts f and q to represent the flaring and quiescent states, respectively.

4.1. Simultaneous SED and Spectropolarimetry Fit Results

The results of the simultaneous SED and degree of polarization fit to the observations of 4C+01.02 in its flaring and quiescent states in 2016 and 2017, respectively, are plotted in Figure 6 with the corresponding fit parameters and quantities derived from the fit parameters shown in Table 2. The low-energy SED components are shown in the left panels where the total flux (contributed by the synchrotron, AD, and BLR line flux components) is fitted through the optical LCO photometry data in the B, V, and R filters for the flaring state and the data in the B, V, R, I filters for the quiescent state (the I-filter data point is not visible in the plots to the right as it is not in the polarization data regime). The right panels show the SED and degree of polarization components in the optical/UV regime. The decrease in the total degree of polarization (due to the unpolarized AD emission diluting the synchrotron emission
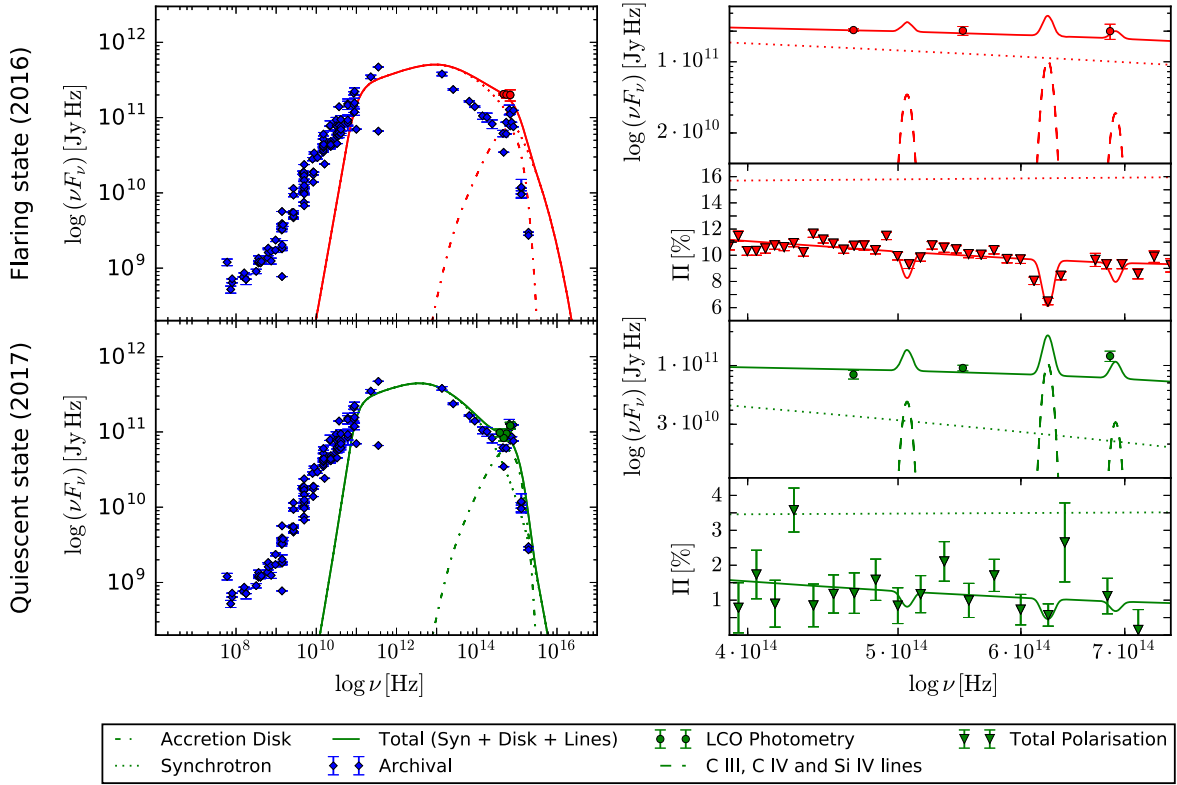
Figure 6. The simultaneous low-energy SED and spectropolarimetry model (lines) fitted to the observations (data points) of 4C+01.02 in its flaring state of 2016 (top panels, red) and quiescent state of 2017 (bottom panels, green). The SEDs are plotted in the left panels, and the SEDs and degree of polarization components in the optical/UV frequency range are plotted in the right panels. Model components and observational data are shown in the legend.

toward higher optical frequencies) constrains the AD component, thereby disentangling the AD flux component and the synchrotron flux component. By constraining the AD component during the quiescent state the BH mass of 4C+01.02 is determined as $\sim 3 \times 10^9 \, M_\odot$. This obtained BH mass was also adopted in the flaring state. When archival UV observations are not taken into account during the quiescent-state model fit, a lower BH mass of $4 \times 10^8 \, M_\odot$ is obtained (Böttcher et al. 2017).

The spectropolarimetry fits clearly show the decrease of the polarization at the frequencies of the unpolarized C III, C IV, and Si IV emission lines. It is assumed that the emission-line fluxes do not change significantly from the flaring to the quiescent state, as the emission-line flux in the quiescent state is poorly constrained.

The radio data are not fitted due to the steepening of the one-zone synchrotron spectrum below the SSA critical frequency at $\nu_{SSA} \sim 2 \times 10^{11}$ Hz for both flaring and quiescent states. The higher optical flux in the flaring state is achieved through a larger synchrotron emission component. Note that the electron spectrum normalization constant n_0 represents the differential number of electrons at γ_b, where γ_b is significantly larger in the flaring-state fit compared to the quiescent-state fit. Thus, the fit parameters imply a larger number of high-energy electrons in the flaring state.

The AD luminosity is obtained through the model fit as $L_{AD}^{M,f} = 4.5 \times 10^{46}$ erg s^{-1} and $L_{AD}^{M,q} = 3.7 \times 10^{46}$ erg s^{-1} for the flaring and quiescent states, respectively. The corresponding maximum temperatures $T_{max}^{M,f} = 3.5 \times 10^4$ K and $T_{max}^{M,q} = 3.4 \times 10^4$ K of the AD near the innermost

stable circular orbit yield a peak frequency of $\nu_{T,max}^{M,f} = 6.6 \times 10^{14}$ Hz and $\nu_{T,max}^{M,q} = 6.3 \times 10^{14}$ Hz for the flaring and quiescent states, respectively, which is dependent on the AD luminosity and BH mass through Equation (3).

Both states necessitated a partially ordered magnetic field with $F_B < 1$. The higher ordering of the magnetic field in the flaring state $F_B^{M,f} = 0.188$ indicates a 4.7 fold increase of the magnetic field ordering parameter compared to the quiescent state, where $F_B^{M,q} = 0.040$.

The χ^2 values per degree of freedom n for the degree of total polarization fit are $(\chi^2/n)_{pol}^{M,f} = 2.88$ and $(\chi^2/n)_{pol}^{M,q} = 1.46$. These values appear acceptable when keeping in mind that additional features in the spectrum have not been included in the model fit such as additional faint emission lines and possibly absorption lines, and a dusty torus that may yield a small contribution in diluting the synchrotron polarization. In this first exploration of combined SED and spectropolarimetry fitting, we fit only the jet synchrotron continuum, the direct AD emission, and the most prominent emission lines.

4.2. Broadband Spectral Energy Distribution

The electron distribution obtained during the model fit (Table 2) was subsequently used as parameters in the Böttcher et al. (2013) code to model the X-ray and gamma-ray emission resulting from SSC and EC scattering. The resulting broadband SED fits are plotted in Figure 7 with parameters as listed in Table 3.

The emission region radius is kept the same between the flaring and quiescent states in order to reduce the number of varying parameters.

Parameters	Flaring State	Quiescent State
Input Parameters		
Magnetic field B [G] at emission region height	0.82	0.82
Bulk Lorentz factor Γ	15	15
Emission region radius R_{em} [cm]	3.0×10^{17}	3.0×10^{17}
Parameters Obtained with Fit		
Normalization factor n_0	3.3×10^{49}	1.1×10^{50}
Minimum gamma γ_{min}	54.8	24.5
Gamma break γ_b	7.27×10^2	4.90×10^2
Critical gamma γ_c	3.00×10^3	1.51×10^3
Electron spectral index p_1	2.62	2.60
Electron spectral index p_2	3.00	3.00
Ordering of magnetic field F_B	0.188	0.040
Disk luminosity L_{AD} [erg s^{-1}]	4.5×10^{46}	3.7×10^{46}
BH mass $[M_\odot]$	$\sim 3 \times 10^9$	$\sim 3 \times 10^9$
C IV line flux h_2 [Jy Hz]	1.0×10^{11}	-
Calculated Values		
Minimum frequency ν_{min} [Hz]	5.0×10^{10}	1.0×10^{10}
Break frequency ν_b [Hz]	8.8×10^{12}	4.0×10^{12}
Critical frequency ν_c [Hz]	1.5×10^{14}	3.8×10^{13}
Photon spectral index α_1	0.81	0.80
Photon spectral index α_2	1.00	1.00
Maximum synchrotron polarization $\Pi_{max}^{syn}(p_1)$	0.73	0.73
Maximum synchrotron polarization $\Pi_{max}^{syn}(p_2)$	0.75	0.75
Maximum disk temperature $T_{AD, max}$ [K]	3.5×10^4	3.4×10^4
$\nu_{T,max}$ [Hz]	6.6×10^{14}	6.3×10^{14}
Goodness of fit $(\chi^2/n)_{pol}$	2.88	1.46
C III line flux h_1 [Jy Hz]	4.8×10^{10}	4.8×10^{10}
C IV line flux h_2 [Jy Hz]	$\cdots$	1.0×10^{11}
Si IV line flux h_3 [Jy Hz]	3.1×10^{10}	3.1×10^{10}

Note. The electron distribution in the emission frame has characteristic Lorentz factors γ, and the characteristic synchrotron radiation profile frequencies are defined in the observer frame.

Our fits suggest a decreasing accretion rate from the flaring to the quiescent state. The fits further require that the emission region is placed slightly farther down the jet in the quiescent state compared to the flaring state, which could lead to a suppressed EC (AD) component and could also be consistent with the lower energy density of the BLR radiation field ($u^{M,q} = 5.5 \times 10^{-4}$ erg cm^{-3} for the quiescent state compared to the flaring state's $u^{M,f} = 9.0 \times 10^{-3}$ erg cm^{-3}).

The dominant EC (BLR) flux component during the flaring state suggests that the emission region is within the BLR, providing an approximately isotropic energy density. During the quiescent state, the EC (BLR) flux component is suppressed, suggesting that the emission region is located at or beyond the outer boundary of the BLR.

4.3. Comparison to Previous Work

Previous works modeling 4C+01.02 were of Ghisellini et al. (2011) and Paliya et al. (2017) considering model fits to SED observations, without including any polarization degree

information. Ghisellini et al. (2011) considered a model fit to SED observations with optical emission being strongly dominated by an AD. Ghisellini et al. (2011) and Paliya et al. (2017) inferred $M_{BH} \sim 5 \times 10^9 M_\odot$. In order to test whether flaring- and/or quiescent-state spectropolarimetry data can safely exclude a larger BH mass, we fixed the BH mass in our fit routine to their obtained BH mass of $\sim 5 \times 10^9 M_\odot$ and attempted SED and spectropolarimetry fits. The parameters and inferred quantities are listed in Table 4, and the resulting low-frequency SED and spectropolarimetry fits are shown in Figure 8.

During the flaring state of 4C+01.02, the IR–optical–UV spectrum is expected to be dominated by the jet synchrotron emission and not the AD emission. The quiescent state may be AD dominated with a low ordered magnetic field in the jet emission region.

Our model, using our best-fit BH mass and that of Ghisellini et al. (2011) and Paliya et al. (2017; their results are indicated by a superscript C) produces AD flux components peaking at $\nu_{T,max}^{M,f} = 6.6 \times 10^{14}$ Hz and $\nu_{T,max}^{M,q} = 6.3 \times 10^{14}$ Hz, and $\nu_{T,max}^{C,f} = 5.3 \times 10^{14}$ Hz and $\nu_{T,max}^{C,q} = 5.1 \times 10^{14}$ Hz , respectively. The degree of total polarization, thereby, decreases at lower frequencies, as demonstrated by Figure 8, second and fourth right panels.

The reduced chi-square χ^2/n values for the fits to n amount of spectropolarimetry data points are $(\chi^2/n)_{pol}^{C,f} = 3.13$ and $(\chi^2/n)_{pol}^{C,q} = 1.54$, compared to $(\chi^2/n)_{pol}^{M,f} = 2.88$ and $(\chi^2/n)_{pol}^{M,q} = 1.46$. This demonstrates that spectropolarimetry data disentangle the synchrotron and AD SED flux components (left in Figure 8) and determine the ordering of the magnetic field. The BH mass obtained by Ghisellini et al. (2011) and Paliya et al. (2017) cannot be excluded.

4.4. BH Mass Estimate Based on the C IV Line Width and Continuum Luminosity

We here provide an independent estimate of the BH mass, following the C IV-based BH mass estimator as recently extended by Park et al. (2017). Their Equation (4) allows a BH mass estimate based on the FWHM of the C IV $\lambda1549$ emission line (in units of km/s) and the AD continuum luminosity at a rest-frame wavelength of 1350 Å. The latter corresponds to an observed frequency of $\nu_{obs}^{cont} = 7.2 \times 10^{14}$ Hz. From our SED fitting, we find an AD continuum $\nu F_\nu = \lambda F_\lambda$ flux of 4.2×10^{-13} erg cm^{-2} s^{-1} at that frequency, corresponding to a rest-frame luminosity of $\lambda L_\lambda = 4\pi d_L^2 \nu F_\nu = 1.3 \times 10^{46}$ erg s^{-1}, where we used a luminosity distance of $d_L = 4.95 \times 10^{28}$ cm.

Fitting a Lorentzian profile to the C IV emission line in our SALT spectra, we obtain an FWHM of $\Delta\lambda_{2016} = 109$ Å for the observation of 2016 July 9 and $\Delta\lambda_{2017} = 90$ Å for the observation of 2017 July 25. We therefore use $\Delta\lambda_{ave} = 100$ Å as a representative average value, corresponding to a velocity of FWHM(C IV) $= 6250$ km s^{-1}.

Plugging these values into Equation (4) of Park et al. (2017), we find $\log(M_{BH}/M_\odot) = 8.9_{-0.53}^{+0.54}$. In the evaluation of this expression, the systematic error of the M_{BH}–L_{1350}–FWHM(C IV) relation greatly dominates over the measurement uncertainties, as the latter are small and only enter logarithmically. We therefore only account for the systematic errors, which are quoted as 1σ uncertainties. The logarithm above then
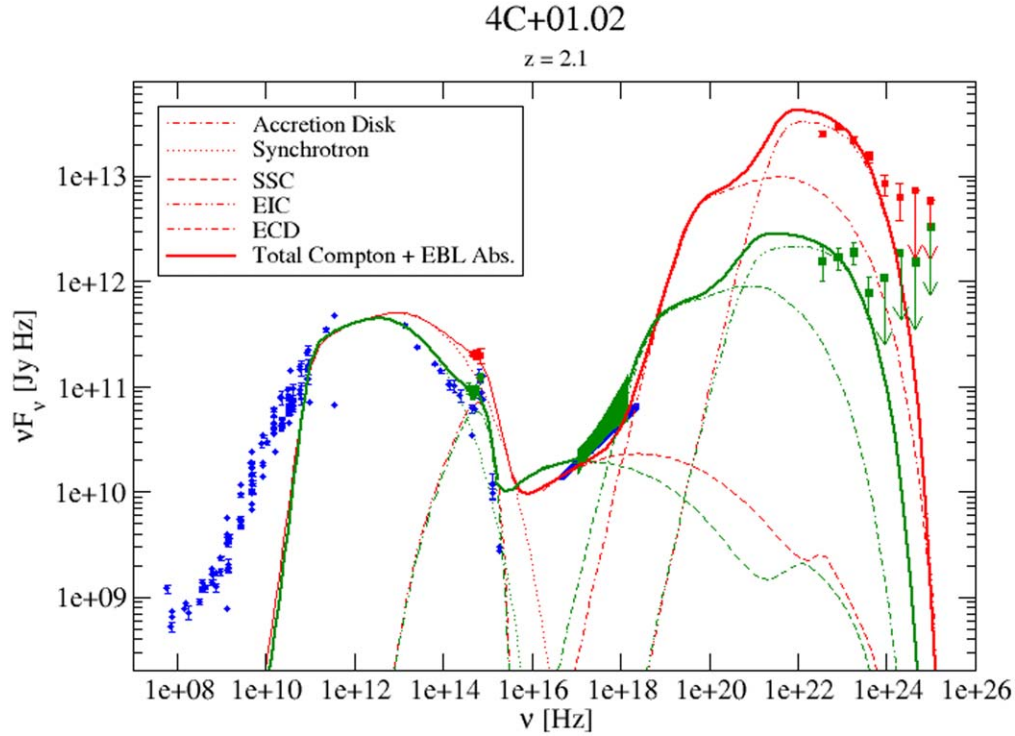
Figure 7. Broadband SED of 4C+01.02 during its flaring (red) and quiescent (green) states by the implementation of the low-energy parameters obtained during the model fit (given in Table 2) into the code of Böttcher et al. (2013) to produce the X-ray and gamma-ray components for a leptonic model. Data from observations are as follow archival data points (blue), LCO photometry data points for the flaring (red) and quiescent (green) states, Swift-XRT data points for the flaring (blue) and quiescent (green) states, and Fermi-LAT data points for the flaring (red) and quiescent (green) states.

Table 3
Parameters Obtained by Implementation of the Low-energy Parameters Constrained with the Simultaneous SED and Polarization Model (Table 2) in the Böttcher et al. (2013) Code to Predict the X-ray and Gamma-ray Components of the Leptonic Model in Figure 7

Parameters	Flaring State	Quiescent State
Input Parameters		
Kinetic luminosity in jet electrons [erg s^{-1}]	3.2×10^{45}	6.0×10^{45}
Emission region height z_0 [pc]	0.15	0.30
Observing angle $\theta_{\mathrm{obs}} = 1/\Gamma$ [°]	3.5	3.5
External radiation field energy density u [erg cm^{-3}]	9.0×10^{-3}	5.5×10^{-4}
External radiation field blackbody temperature [K]	5×10^4	5×10^4
Derived Parameters		
$L_B(jet)$ [erg s^{-1}]	5.1×10^{46}	5.1×10^{46}
L_B/L_e	16.0	8.51
$dt_{\mathrm{var,min}}$	1.9×10^6 s	1.9×10^6 s
	$= 5.3 \times 10^2$ hr	$= 5.3 \times 10^2$ hr

corresponds to

$$M_{\mathrm{BH}} = (7.7 \times 10^8)^{+2.2 \times 10^9}_{-5.4 \times 10^8} \, M_{\odot}. \qquad (7)$$

The BH mass of $\sim 3 \times 10^9 \, M_{\odot}$ as found through our SED and spectropolarimetry fitting is consistent with the upper limit, while the mass of $\sim 5 \times 10^9 \, M_{\odot}$ used by Ghisellini et al. (2011) and Paliya et al. (2017) is further outside the 1σ error interval. If one interpreted the entire observed flux at 7.2×10^{14} Hz during the quiescent state as accretion disk flux, the best

estimate would increase to $\sim 1.2 \times 10^9 \, M_{\odot}$, with the upper limit of the 1σ error range increasing to $4.2 \times 10^9 \, M_{\odot}$.

Thus, we conclude that this independent black hole mass estimate favors the value of $M_{\mathrm{BH}} \sim 3 \times 10^9 \, M_{\odot}$ from our SED and spectropolarimetry fitting.

5. Summary and Conclusions

In this paper we describe the development of a code to simultaneously fit the low-frequency SED and spectropolarimetry data of blazars. The model was applied to the blazar 4C +01.02, comparing contemporaneous optical LCO photometry and SALT spectropolarimetry data during a flaring and a quiescent state in 2016 and 2017, respectively. The model assumes an unpolarized AD diluting the degree of electron synchrotron polarization toward higher frequencies and by disentangling the synchrotron and AD components, the AD component and the BH mass are constrained. With our model fits, we could determine the BH mass of 4C+01.02 as $\sim 3 \times 10^9 \, M_{\odot}$.

The magnetic field ordering determines the synchrotron polarization degree and can be determined with spectropolarimetry observations. This parameter will also determine the degree of high-energy polarization due to synchrotron self-Compton scattering in the X-ray and gamma-ray regimes.

The highly ordered magnetic field $F_B^{M,f} = 0.188$ during the flaring state, compared to the quiescent state's $F_B^{M,q} = 0.040$, indicates a localized emission region possibly representing the passing of a shock. Shocks enhance, compress, and order the magnetic fields in the jet, and thereby higher synchrotron and SSC flux components are obtained from the jet. However, higher EC (AD) and EC (BLR) flux components are not dependent on magnetic field ordering. These components might

Table 4
Parameters Obtained and Values Calculated by Implementing the BH Mass of $\sim 5 \times 10^9 \, M_\odot$ Obtained for 4C+01.02 by Ghisellini et al. (2011) and Paliya et al. (2017)

Parameters	Flaring State	Quiescent State
Input Parameters		
Magnetic field B [G] at emission region height	0.82	0.82
Bulk Lorentz factor Γ	15	15
Emission region radius $R_{\rm em}$ [cm]	3.0×10^{17}	3.0×10^{17}
Parameters Obtained with Fit		
Normalization factor n_0	3.9×10^{49}	1.3×10^{50}
Minimum gamma $\gamma_{\rm min}$	54.8	24.5
Gamma break $\gamma_{\rm b}$	7.26×10^2	4.88×10^2
Critical gamma $\gamma_{\rm c}$	2.45×10^3	1.24×10^3
Electron spectral index p_1	2.50	2.33
Electron spectral index p_2	3.00	3.00
Ordering of magnetic field F_B	0.21	0.053
Disk luminosity $L_{\rm AD}$ [erg s^{-1}]	5.2×10^{46}	4.4×10^{46}
C IV line flux h_2 [Jy Hz]	1.0×10^{11}	-
Calculated Values		
Minimum frequency $\nu_{\rm min}$ [Hz]	5.0×10^{10}	1.0×10^9
Break frequency $\nu_{\rm b}$ [Hz]	8.8×10^{12}	4.0×10^{12}
Critical frequency $\nu_{\rm c}$ [Hz]	1.0×10^{14}	2.5×10^{13}
Photon spectral index α_1	0.75	0.66
Photon spectral index α_2	1.00	1.00
Maximum synchrotron polarization $\Pi_{\rm max}^{\rm syn}(p_1)$	0.72	0.71
Maximum synchrotron polarization $\Pi_{\rm max}^{\rm syn}(p_2)$	0.75	0.75
Maximum disk temperature $T_{AD, \rm max}$ [K]	2.8×10^4	2.7×10^4
$\nu_{T, \rm max}$ [Hz]	5.3×10^{14}	5.1×10^{14}
Goodness of fit $(\chi^2/n)_{pol}$	3.15	1.53
C III line flux h_1 [Jy Hz]	4.8×10^{10}	4.8×10^{10}
C IV line flux h_2 [Jy Hz]	$\cdots$	1.0×10^{11}
Si IV line flux h_3 [Jy Hz]	3.1×10^{10}	3.1×10^{10}

Note. These results correspond to Figure 8 where the AD components was shifted during the flaring and quiescent states to enable a fit.

be enhanced because particles are accelerated more efficiently. A higher/lower synchrotron flux component means that there are more/fewer available photons to produce a higher/lower SSC flux component in the flaring/quiescent state.

The less ordered magnetic field in the quiescent state suggests the presence of more tangled magnetic fields where magnetic field reconnection can take place and magnetic field orientations in different directions cancel each other out. These lead to a lower degree of synchrotron polarization.

A fit to the low-frequency (synchrotron + AD + BLR) emission components alone cannot independently constrain electron energies, magnetic field, and the size of the emission region. Additional constraints on those parameters result from a fit to the entire SED, which was subsequently performed using the code of Böttcher et al. (2013). The resulting fits suggest that SSC, EC (AD), and EC (BLR) are all contributing significantly to the X-ray through gamma-ray emission of 4C+01.02 and that the emission region is likely to be located further out along the jet in the quiescent state, compared to the flaring state.

The BH mass of $\sim 3 \times 10^9 \, M_\odot$, obtained with our model fits, is inconsistent with that of Ghisellini et al. (2011) and

Paliya et al. (2017) who obtained the BH mass for this source as $\sim 5 \times 10^9 \, M_\odot$ by fitting the SED. Our BH mass estimate is consistent with the upper limit of the C IV-based BH estimation following the method developed by Park et al. (2017). According to a simultaneous fit to the SED and spectro-polarimetry data, the BH mass obtained by Ghisellini et al. (2011) and Paliya et al. (2017) cannot be ruled out.

Both our own model and the models of Ghisellini et al. (2011) and Paliya et al. (2017) considered a Shakura & Sunyaev (1973) AD model assuming a nonrotating BH. However, if the AD is considered truncated at the innermost stable orbit and the BH is considered to rotate retrograde/prograde to the AD, the disk moves farther out/closer to the BH. The maximum disk temperature then decreases/increases, giving the impression of a larger/smaller BH mass. Because both models used the same AD prescription based on a nonrotating BH, BH rotation cannot be invoked to resolve the discrepancy in the inferred BH mass values. The BH mass inferred by Ghisellini et al. (2011) and Paliya et al. (2017) results in an AD component at lower frequencies in the EM spectrum. If we take into account that in their model Paliya et al. (2017) used $\epsilon \sim 1/10$ compared to our $\epsilon \sim 1/12$, their AD component moves to lower $\nu_{T, \rm max}$ and lower fluxes when considering lower $\epsilon \sim 1/12$, because $\nu_{T, \rm max} \propto \epsilon^{1/4}$. This will, therefore, not provide a shift of their AD component to higher frequencies and does not explain the discrepancy (Calderone et al. 2013).

In future work, we will extend our model to include high-energy (Compton) emission in the same fitting routine, including predictions for X-ray and gamma-ray polarization, and include potential hadronic high-energy emission components, similar to the work of Zhang & Böttcher (2013) and Paliya et al. (2018). The inclusion of inverse Compton (IC) components will enable further constraints on the emission region parameters and dominant emission mechanisms. Predictions will be made for the Future Imaging X-ray Polarimetry Explorer (IXPE; Weisskopf et al. 2016) spacecraft that is scheduled for launch in 2021[16] and the All-sky Medium Energy Gamma-ray Observatory (AMEGO)[17] for gamma-ray polarimetry.

SALT ToO observations and coordinated multiwavelength observations are continuing so that more sources (including BL Lacs) will be available for combined SEDs and spectro-polarimetry fitting.

In the case of 4C+01.02 considered here, the host galaxy and a putative dusty torus do not contribute significantly to the observed SED. However, for the purpose of fitting other sources, these contributions will be included in our model as additional unpolarized emission components in future work.

POLLUX, a UV polarimeter aboard the Large UV/Optical/Infrared Surveyor (LUVOIR), has been proposed as a Concept Study to the 2020 Decadal Survey which could provide UV polarization data to further constrain the AD components in blazar SEDs toward UV frequencies (Bouret et al. 2018; Marin et al. 2018).
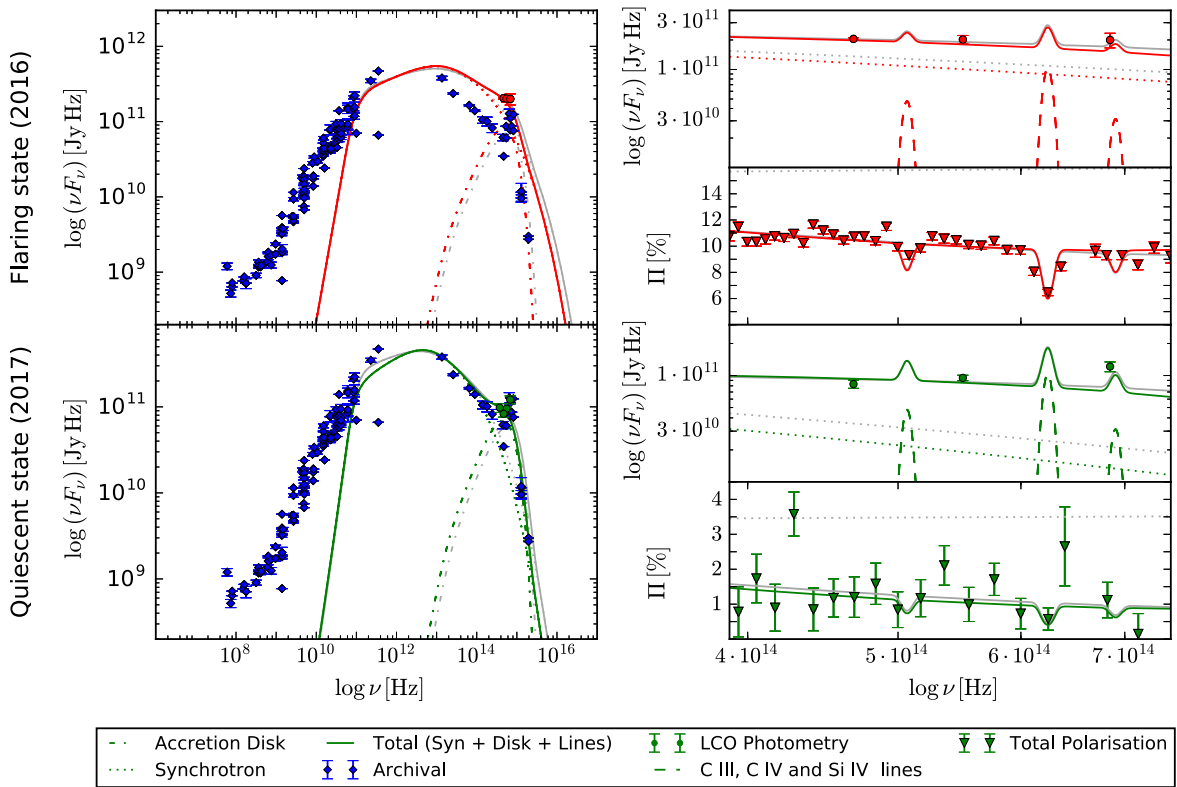

Figure 8. Implementation of the BH mass obtained for 4C+01.02 as $\sim 5 \times 10^9\, M_\odot$ by Ghisellini et al. (2011) and Paliya et al. (2017) in our simultaneous SED and spectropolarimetry model. Parameters obtained during this model fit and calculated values are given in Table 4. The model fit obtaining a BH mass of $\sim 3 \times 10^9\, M_\odot$ is shown in gray.

ORCID iDs

Hester M. Schutte ● https://orcid.org/0000-0002-1769-5617
Richard J. Britto ● https://orcid.org/0000-0003-3456-2362
Markus Böttcher ● https://orcid.org/0000-0002-8434-5692
Brian van Soelen ● https://orcid.org/0000-0003-1873-7855
Johannes P. Marais ● https://orcid.org/0000-0002-4009-713X
Amanpreet Kaur ● https://orcid.org/0000-0002-0878-1193
Abraham D. Falcone ● https://orcid.org/0000-0002-5068-7344
David A. H. Buckley ● https://orcid.org/0000-0002-7004-9956
Andry F. Rajoelimanana ● https://orcid.org/0000-0002-9359-2214
Justin Cooper ● https://orcid.org/0000-0002-6068-4737

References

Abdo, A. A., Ackermann, M., Ajello, M., et al. 2011, ApJL, 733, L26
Aharonian, F. A. 2000, NewA, 5, 377
Arnaud, K. A. 1996, in ASP Conf. Ser., 101, Astronomical Data Analysis Software and Systems V, ed. G. H. Jacoby & J. Barnes (San Francisco, CA: ASP), 17
Atwood, W., Albert, A., Baldini, L., et al. 2013, arXiv:1303.3514
Atwood, W. B., Abdo, A. A., Ackermann, M., et al. 2009, ApJ, 697, 1071
Böttcher, M., Reimer, A., Sweeney, K., & Prakash, A. 2013, ApJ, 768, 54
Böttcher, M., van Soelen, B., Britto, R., et al. 2017, Galax, 5, 52
Bouret, J.-C., Neiner, C., Gómez de Castro, A. I., et al. 2018, Proc. SPIE, 10699, 106993B
Brink, J. D., Buckley, D. A. H., Nordsieck, K. H., & Potter, S. B. 2010, Proc. SPIE, 7735, 773517
Britto, R. J., Bottacini, E., Lott, B., Razzaque, S., & Buson, S. 2016, ApJ, 830, 162
Britto, R. J., Marais, J. P., Meintjes, P. J., et al. 2017, PoS, 2017, 21
Buckley, D. A. H., Swart, G. P., & Meiring, J. G. 2006, Proc. SPIE, 6267, 62670Z
Burgh, E. B., Nordsieck, K. H., Kobulnicky, H. A., et al. 2003, Proc. SPIE, 4841, 1463
Burrows, D. N., Hill, J. E., Nousek, J. A., et al. 2005, SSRv, 120, 165

Calderone, G., Ghisellini, G., Colpi, M., & Dotti, M. 2013, MNRAS, 431, 210
Cash, W. 1979, ApJ, 228, 939
Crawford, S. M., Still, M., Schellart, P., et al. 2010, Proc. SPIE, 7737, 773725
Dermer, C. D., & Schlickeiser, R. 1993, ApJ, 416, 458
Finke, J. D., Razzaque, S., & Dermer, C. D. 2010, ApJ, 712, 238
Francis, P. J., Hewett, P. C., Foltz, C. B., et al. 1991, ApJ, 373, 465
Gaia Collaboration 2018, yCat, I/345
Gehrels, N., Chincarini, G., Giommi, P., et al. 2004, ApJ, 611, 1005, [Erratum: 2005, ApJ, 621, 558]
Ghisellini, G., Tagliaferri, G., Foschini, L., et al. 2011, MNRAS, 411, 901
Jordi, K., Grebel, E. K., & Ammon, K. 2006, A&A, 460, 339
Kalberla, P. M. W., Burton, W. B., Hartmann, D., et al. 2005, A&A, 440, 775
Kobulnicky, H. A., Nordsieck, K. H., Burgh, E. B., et al. 2003, Proc. SPIE, 4841, 1634
Longair, M. S. 2011, High Energy Astrophysics (Cambridge: Cambridge Univ. Press)
Mannheim, K. 1993, A&A, 269, 67
Marin, F., Charlot, S., Hutsemékers, D., et al. 2018, in SF2A-2018: Proc. Annual meeting of the French Society of Astronomy and Astrophysics, ed. P. Di Matteo et al. (Paris: SF2A), 71
Marscher, A. P., & Gear, W. K. 1985, ApJ, 298, 114
McCully, C., Volgenau, N. H., Harbeck, D.-R., et al. 2018, Proc. SPIE, 10707, 107070K
Meyer, E. T., Fossati, G., Georganopoulos, M., & Lister, M. L. 2012, ApJL, 752, L4
Mücke, A., Protheroe, R. J., Engel, R., Rachen, J. P., & Stanev, T. 2003, APh, 18, 593
Nasa High Energy Astrophysics Science Archive Research Center (Heasarc) 2014, HEAsoft: Unified Release of FTOOLS and XANADU, Astrophysics Source Code Library, ascl:1408.004
Nordsieck, K. 2012, in AIP Conf. Ser., 1429, American Institute of Physics Conference Series, ed. J. L. Hoffman, J. Bjorkman, & B. Whitney (Melville, NY: AIP), 248
Paliya, V. S., Marcotulli, L., Ajello, M., et al. 2017, ApJ, 851, 33
Paliya, V. S., Zhang, H., Böttcher, M., et al. 2018, ApJ, 863, 98
Pâris, I., Petitjean, P., Aubourg, É., et al. 2018, A&A, 613, A51
Park, D., Barth, A. J., Woo, J.-H., et al. 2017, ApJ, 839, 93
Potter, S. B., Nordsieck, K., Romero-Colmenero, E., et al. 2016, Proc. SPIE, 9908, 99082K
Rybicki, G. B., & Lightman, A. P. 1986, Radiative Processes in Astrophysics (New York: Wiley)
Shakura, N. I., & Sunyaev, R. A. 1973, A&A, 24, 337
Sikora, M., Begelman, M. C., & Rees, M. J. 1994, ApJ, 421, 153
Smith, P. S., Balonek, T. J., Heckert, P. A., & Elston, R. 1986, ApJ, 305, 484
Stickel, M., Padovani, P., Urry, C. M., Fried, J. W., & Kuehr, H. 1991, ApJ, 374, 431
Verrecchia, F., Lucarelli, F., Pittori, C., et al. 2016, ATel, 9232, 1
Weisskopf, M. C., Ramsey, B., O'Dell, S. L., et al. 2016, ResPh, 6, 1179
Westfold, K. C. 1959, ApJ, 130, 241
Zhang, H., & Böttcher, M. 2013, ApJ, 774, 18